Research paper

WEC spacing effects on the performance of a floating energy harvesting platform

Haitao Wu , Zhiming Yuan [*]

Department of Naval Architecture, Ocean and Marine Engineering, University of Strathclyde, Glasgow, G4 0LZ, United Kingdom

ARTICLE INFO

ABSTRACT

This paper proposes a floating energy harvesting platform concept, which integrates multiple point-absorber wave energy converters (WECs) onto a floating semi-submersible platform. The focus is to investigate WEC spacing effects on the dynamic response and energy harvesting performance of the hybrid system. To this end, five energy harvesting models with various WEC spacings are defined. Under average wave height condition, the typical wave periods are considered to analyze the performance variations in these models. Notably, the influence of hydrodynamic interactions is evaluated on the energy absorption. Furthermore, under both average and severe wave conditions, the present study establishes different performance evaluation criteria and conducts comparative analysis across the models. The results indicate that under average wave condition, the optimal energy harvesting model varies depending on the evaluation benchmark. Additionally, under severe wave condition, the model with the smallest WEC spacing demonstrates the best performance. Overall, the present study emphasizes the effects of the hydrodynamic interactions on the performance of the wave-energy integrated system, of which the analytical framework and methods could provide some insights into the design and optimization of other ocean energy systems.

1. Introduction

Replacing traditional fossil fuels with renewable energy can significantly accelerate the goal of achieving a carbon-neutral world by 2050 (Shi et al., 2022). Wherein, ocean energy is a crucial focus area for exploiting renewable energy. It is worth noting that wind energy, wave energy, tidal energy, and photovoltaic energy are the four primary types of ocean energy. Among them, wave energy is considered the most promising due to its higher energy density and capability for continuous operation (Cui et al., 2024). The theoretical amount of global wave energy resource is extremely huge (Gunn and Stock-Williams, 2012), highlighting its potential to expedite the decarbonization of global electricity supply.

After years of development, five main types of WECs have emerged: oscillating water column (OWC), bottom-hinged, overtopping, point-absorber, and multi-body hinged devices (Wu et al., 2024a). Among them, the point-absorber WECs have garnered significant attention from academia and industry because of the outstanding energy conversion efficiency, minimal environmental impact, low construction and installation costs, and flexible deployment configurations (Wu et al., 2024a).

Furthermore, a common approach to capturing more wave energy is incorporating multiple WECs into a wave farm (Kamarlouei et al., 2020). A bottom-moored platform can serve as the carrier for a wave farm, enhancing its stability, reliability, and cost-effectiveness (Li and Yu, 2012; Nguyen et al., 2020). In the past decade, many researchers have conducted the experimental and numerical studies on the hybrid concepts that combine the platform and point-absorber WECs. Ghafari et al. (2022) assessed the impact of WEC properties on the dynamic response of a Wavestar WEC and semi-submersible platform hybrid system. The findings indicated that the energy capture of the WEC array was much reduced by the hydrodynamic interactions under large wave periods. Zhou et al. (2023) analyzed the performance of a heaving WEC and Spar wind turbine integrated system and found that incorporating WECs affected the platform motion insignificantly but rather improved its rotational stability. Wu and Yuan, 2024 evaluated the effects of three WEC shapes on the performance of a wind-wave hybrid concept, concluding that truncated conical WEC was the most beneficial design. Cheng et al. (2022) integrated oscillating body (OB) and OWC WECs into a WEC-breakwater hybrid system, conducting a series of experimental

---

and numerical studies to explore its energy harvesting and wave attenuation mechanisms. They discovered that the integrated device outperformed the single OB or OWC WECs in energy harvesting and wave attenuation. Zhao et al. (2023) utilized the hydrodynamic and structural dynamics to study the hydroelastic response and energy capture of a WEC-platform hybrid system in the frequency domain. The findings suggested that neglecting hydroelasticity could lead to an overestimation of energy absorption within certain wavelength ranges. Ding et al. (2024) performed fully coupled analysis to assess the impact of different WEC layouts on the dynamic behavior of a WEC-barge platform integrated system. They concluded that an appropriate WEC layout could enhance the power output and improve the platform stability. Gu et al. (2025) evaluated the performance of a semi-submersible wind turbine and oscillating-body WEC hybrid system, showing that the integrated concept significantly increased the power output but was more sensitive to the wave excitations. Rony and Karmakar (2024) studied the effects of WEC array configurations on the hydrodynamic behavior of a heaving WEC and tension leg platform hybrid system. The findings showed that the integrated concept could suppress the platform motion and enhance the energy absorption. Sun et al. (2021) conducted experimental studies on the WEC-platform system under regular and irregular wave conditions, observing that the addition of WECs could suppress the platform pitch motion in certain cases but increased the heave and pitch responses. He et al. (2023) adopted the numerical simulations to analyze the impact of the platform response on the energy capture of the point-absorber WEC array. The results implied that the heave response was favorable for the energy capture of the WEC array, while the situation was reversed for the pitch response. Chen et al. (2024) evaluated the influence of the WEC configurations on the hydrodynamics of a wave-wind hybrid concept, concluding that the WEC increase improved the system stability under realistic sea states. Zhang et al. (2023) utilized the experimental study on the hydrodynamic response of a split heaving WEC and tension leg platform integrated system, finding that shallow-water effects and out-of-phase heave motion increased the energy capture of the split WEC.

Although the WEC layout has been addressed in numerous works, the influence of hydrodynamic interactions on the performance of the WEC-platform systems are still not understood well. Moreover, establishing reasonable performance evaluation criteria is crucial for different WEC array configurations. It is worth noting that the evaluation criterion under operational wave conditions should differ from that under extreme wave conditions. This paper proposes a floating energy harvesting platform concept, considering five different WEC spacings. The current study adopts the numerical analysis on the dynamic behavior of this hybrid system, addressing the two aforementioned challenges. The results and analytical framework presented in this paper could provide some reference values for the design and optimization of other ocean energy devices.

2. Theoretical background

2.1. Hydrodynamic forces and coefficients

Potential flow theory assumes that the fluid field around the body is incompressible, irrotational, and inviscid. The velocity potential includes the incident potential φ_I, diffraction potential φ_D, and radiation potential φ_R (Barltrop, 1988):

$$\varphi(x,y,z)e^{-i\omega t} = \left[(\varphi_I + \varphi_D) + \sum_{j=1}^{6} \varphi_{Rj} x_j \right] e^{-i\omega t}, j = 1 \sim 6 \tag{1}$$

where φ_{Rj} is the radiation potential due to x_j, which represents the motion amplitude of the j-th degree of freedom (DOF).

φ_I can be expressed as:

$$\varphi_I = -i\frac{Ag}{\omega} \frac{\cos h[k(z+d)]}{\cos h(kd)} e^{ik(x\cos\beta + y\sin\beta)} \tag{2}$$

where A and ω are the wave amplitude and circular frequency, respectively; g is the gravity acceleration; k is the wave number; d is the water depth; β refers to the wave direction.

The velocity potential must satisfy the Laplace's equation and boundary conditions (Newman, 1979),

$$\begin{cases} \Delta\varphi = \dfrac{\partial^2 \varphi}{\partial x^2} + \dfrac{\partial^2 \varphi}{\partial y^2} + \dfrac{\partial^2 \varphi}{\partial z^2} = 0 \\[2mm] -\omega^2 \varphi + g\dfrac{\partial \varphi}{\partial z} = 0, at\ z = 0 \\[2mm] \dfrac{\partial \varphi_j}{\partial n} = \begin{cases} n_j, j = 1, \dots, 6 \\[1mm] -\dfrac{\partial \varphi_I}{\partial n}, j = 7 \end{cases}, on\ body\ surface \\[3mm] \dfrac{\partial \varphi}{\partial z} = 0, at\ z = -d \\[2mm] \lim_{r \to \infty} \sqrt{r}\left(\dfrac{\partial \varphi}{\partial r} - ik\varphi \right) = 0, at\ r = \sqrt{x^2 + y^2} \to 0 \end{cases} \tag{3}$$

where $\varphi_7 = \varphi_D$; n is the normal vector of body surface pointing to the fluid field.

The hydrodynamic pressure on the body surface can be expressed as:

$$P = -\rho \frac{\partial \varphi}{\partial t} = i\omega\rho\varphi e^{-i\omega t} \tag{4}$$

where ρ is the density of sea water. Then, the hydrodynamic forces are generalized as:

$$F_j e^{-i\omega t} = -\iint_{S_0} P n_j dS = \left[-i\omega\rho \iint_{S_0} \varphi n_j dS \right] e^{-i\omega t} \tag{5}$$

where S_0 denotes the mean wetted body surface.

Based on Eq. (1), the hydrodynamic forces can be also expressed as:

$$F_j = \left[(F_{Ij} + F_{Dj}) + \sum_{k=1}^{6} F_{Rjk} x_k \right] \tag{6}$$

where F_{Ij} is the Froude-Krilov force, F_{Dj} is the diffraction force, and F_{Rjk} is the radiation force, which is further derived as:

$$F_{Ij} = -i\omega\rho \iint_{S_0} \varphi_I n_j dS \tag{7}$$

$$F_{Dj} = -i\omega\rho \iint_{S_0} \varphi_D n_j dS \tag{8}$$

$$F_{Rjk} = -i\omega\rho \iint_{S_0} \varphi_{Rk} n_j dS \tag{9}$$

Eq. (13) can also be formulated as:

$$F_{Rjk} = -i\omega\rho \iint_{S_0} \{Re[\varphi_{Rk}] + iIm[\varphi_{Rk}]\} n_j dS = \omega\rho \iint_{S_0} Im[\varphi_{Rk}] n_j dS - i\omega\rho \iint_{S_0} Re[\varphi_{Rk}] n_j dS = \omega^2 A_{jk} + i\omega B_{jk} \tag{10}$$

where A_{jk} is the added mass coefficient, and B_{jk} is the radiation damping coefficient, which can be formulated as:

$$A_{jk} = \frac{\rho}{\omega} \iint_{S_0} Im[\varphi_{Rk}] n_j dS \tag{11}$$

$$B_{jk} = -\rho \iint_{S_0} Re[\varphi_{Rk}] n_j dS \tag{12}$$

Under finite water depth condition, the present study employs the frequency-domain pulsating Green's function and the boundary integral method to resolve the velocity potential. In addition to the boundary conditions, the following condition must also be satisfied within the fluid domain (Havelock, 1955):

$$\Delta G(\overrightarrow{p}, \overrightarrow{q}) = \frac{\partial^2 G}{\partial x^2} + \frac{\partial^2 G}{\partial y^2} + \frac{\partial^2 G}{\partial z^2} = \delta(\overrightarrow{p} - \overrightarrow{q}) \tag{13}$$

where $\overrightarrow{p}$ and $\overrightarrow{q}$ are the coordinates of the field point and source point, respectively; δ is the Dirichlet function, which can be formulated as:

$$\delta(\overrightarrow{p} - \overrightarrow{q}) = \begin{cases} 0, \overrightarrow{p} - \overrightarrow{q} \neq 0 \\ \infty, \overrightarrow{p} - \overrightarrow{q} = 0 \end{cases} \tag{14}$$

Meanwhile, the Green's function G can be written as:

$$G(\overrightarrow{p}, \overrightarrow{q}) = \frac{1}{r_1} + \frac{1}{r_2} + \int_0^\infty \frac{2(K+\varepsilon)e^{-Kd} cosh[K(z+d)]cosh[K(z_0+d)]}{K sinh(Kd) - \varepsilon cosh(Kd)} J_0(KR)dK$$
$$+ i2\pi \frac{(k_0+\varepsilon)e^{-k_0 d} cosh[k_0(z+d)]cosh[k_0(z_0+d)]}{sinh(k_0 d) + k_0 d cosh(k_0 d) - \varepsilon d sinh(k_0 d)} J_0(k_0 R) \tag{15}$$

where J_0 is the Bessel function of the first kind, and

$$\overrightarrow{q} = (x_0, y_0, z_0) \tag{16}$$

$$R = \sqrt{(x - x_0)^2 + (y - y_0)^2} \tag{17}$$

$$r_1 = \sqrt{R^2 + (z - z_0)^2} \tag{18}$$

$$r_2 = \sqrt{R^2 + (z + z_0 - 2d)^2} \tag{19}$$

$$\varepsilon = \frac{\omega^2}{g} \tag{20}$$

$$k_0 \tan h(k_0 d) = \varepsilon \tag{21}$$

Based on the Green's theorem, the diffraction and radiation potentials can be derived as the Fredholm integral equation of the second kind,

$$c\varphi(\overrightarrow{p}) = \iint_{S_0} \left\{ \varphi(\overrightarrow{q}) \frac{G(\overrightarrow{p}, \overrightarrow{q})}{\partial n(\overrightarrow{q})} - G(\overrightarrow{p}, \overrightarrow{q}) \frac{\varphi(\overrightarrow{q})}{\partial n(\overrightarrow{q})} \right\} dS \tag{22}$$

where S_0 is the body wetted surface, and

$$c = \begin{cases} 0, \overrightarrow{p} \notin \Omega \cup S_0 \\ 2\pi, \overrightarrow{p} \in S_0 \\ 4\pi, \overrightarrow{p} \in \Omega \end{cases} \tag{23}$$

Meanwhile, the fluid velocity potential can be expressed using the source distribution on the body wetted surface,

$$\varphi(\overrightarrow{p}) = \frac{1}{4\pi} \iint_{S_0} \sigma(\overrightarrow{q}) G(\overrightarrow{p}, \overrightarrow{q}) dS, \overrightarrow{p} \in \Omega \cup S_0 \tag{24}$$

The source strength on the wetted surface can be determined by the body surface boundary condition,

$$\frac{\partial \varphi(\overrightarrow{p})}{\partial n(\overrightarrow{p})} = -\frac{1}{2} \sigma(\overrightarrow{p}) + \frac{1}{4\pi} \iint_{S_0} \sigma(\overrightarrow{q}) \frac{\partial G(\overrightarrow{p}, \overrightarrow{q})}{\partial n(\overrightarrow{p})} dS, \overrightarrow{p} \in S_0 \tag{25}$$

To solve the above equations, the Hess-Smith constant panel method is adopted. This method divides the body wetted surface into quadrilateral or triangular panels. It is assumed that the velocity potential and source strength are constant within each panel, and taken as the corresponding average values over that panel surface. Therefore, the discretized integral forms of Eqs. (24) and (25) can be expressed as (Hess and Smith, 1964):

$$\varphi(\overrightarrow{p}) = \frac{1}{4\pi} \sum_{i=1}^{N_s} \sigma_i G\left(\overrightarrow{p}, \overrightarrow{q}_i\right) \Delta S_i, \overrightarrow{p} \in \Omega \cup S_0 \tag{26}$$

$$\frac{\partial \varphi\left(\overrightarrow{p}_j\right)}{\partial n\left(\overrightarrow{p}_j\right)} = -\frac{1}{2} \sigma_j + \frac{1}{4\pi} \sum_{i=1}^{N_s} \sigma_i \frac{\partial G\left(\overrightarrow{p}_j, \overrightarrow{q}_i\right)}{\partial n\left(\overrightarrow{p}_j\right)} \Delta S_i, \overrightarrow{p}_j \in S_0, j = 1 \sim N_s \tag{27}$$

where N_s is the total number of panels on the body wetted surface; $\overrightarrow{p}_j$ and $\overrightarrow{q}_i$ are the coordinates of the geometric centers of the j-th and i-th panels, respectively; ΔS_i is the area of the i-th panel; σ_i and σ_j are the source strengths of the i-th and j-th panels, respectively.

2.2. Mooring line dynamics

The lumped mass method is used to solve the mooring dynamics (Hall and Goupee, 2015), in which the mooring cable is discretized into multiple nodes connected by massless springs. The equation of motion for each node can be expressed as:

$$(\boldsymbol{m}_i + \boldsymbol{a}_i)\ddot{\boldsymbol{r}}_i = \boldsymbol{T}_i + \boldsymbol{C}_i + \boldsymbol{W}_i + \boldsymbol{B}_i + \boldsymbol{D}_{pi} + \boldsymbol{D}_{qi} \tag{28}$$

where $\boldsymbol{m}$ and $\boldsymbol{a}$ are the mass and added mass matrices of the node, respectively; $\boldsymbol{T}$ is the tension matrix, and $\boldsymbol{C}$ is the internal damping matrix; $\boldsymbol{W}$ represents the gravity force in the water; $\boldsymbol{B}$ is the contact force; $\boldsymbol{D}_p$ and $\boldsymbol{D}_q$ are the normal and tangential drag force matrices, respectively.

2.3. Time-domain motion equation of the hybrid system

The displacement continuity condition must be considered for a floating multi-body connected system, of which the time-domain motion equation can be expressed as (Sun et al., 2011; Cummins, 1962):

$$\begin{bmatrix} \boldsymbol{M} + \boldsymbol{A}(\infty) & \boldsymbol{H}^T \\ \boldsymbol{H} & \boldsymbol{0} \end{bmatrix} \begin{bmatrix} \ddot{\boldsymbol{x}}(t) \\ \boldsymbol{F}_c \end{bmatrix} = \begin{bmatrix} -\int_0^t \boldsymbol{h}(t-\tau)\dot{\boldsymbol{x}}(\tau)d\tau - (\boldsymbol{C}_{vis} + \boldsymbol{C}_{PTO})\dot{\boldsymbol{x}}(t) - \boldsymbol{K}_h \boldsymbol{x}(t) + \boldsymbol{F}_e(t) + \boldsymbol{F}_m(t) \\ \boldsymbol{0} \end{bmatrix} \tag{29}$$

Table 1
Main parameters of the semi-submersible platform.

Parameter	Value
Draft (m)	30
Displacement (kg)	1.64 E7
Mass (kg)	1.61 E7
Center of gravity below MWL (CoG) (m)	9.68
Radius of gyration around x-axis (R_{xx}) (m)	37.00
Radius of gyration around y-axis (R_{yy}) (m)	37.00
Radius of gyration around z-axis (R_{zz}) (m)	20.00

Table 2
Main parameters of the mooring system.

Parameter	Value
Number of mooring lines	6
Angle between adjacent lines (deg)	5
Angle between each group of lines (deg)	120
Fairlead above MWL (m)	15
Anchor below MWL (m)	60
Radius from platform center to fairleads (m)	54.5
Radius from platform center to anchors (m)	830.0
Length of mooring line (m)	800.0
Outer diameter of mooring line (m)	0.120
Mass in water (t/m)	0.303
Axial stiffness (kN)	1.243 E6

Table 3
Main parameters of the WEC.

Parameter	Value
Mass (kg)	1.1136E5
Radius (m)	4
COG below MSL (m)	0
Draft (m)	2
Horizontal distance between hinge point and COG (m)	9.72
Elevation of hinge point above MSL (m)	5.44
Elevation of WEC above MSL (m)	2
Roll inertia (kg • m^2)	6.800E+05
Pitch inertia (kg • m^2)	9.545E+05
Yaw inertia (kg • m^2)	1.054E+06
PTO damping coefficient (N • m • s/rad)	4.100E+07

where $\boldsymbol{M}$ is the mass matrix; $\boldsymbol{A}(\infty)$ is the added mass matrix at infinite frequency; $\boldsymbol{H}$ denotes the constraint matrix; $\boldsymbol{F}_c$ represents the forces caused by the constraints; $\boldsymbol{C}_{vis}$ and $\boldsymbol{C}_{PTO}$ are the linearized viscous and PTO damping matrices, respectively; $\boldsymbol{K}_h$ is the hydrostatic stiffness matrix; $\boldsymbol{F}_e(t)$ denote the wave excitation forces, and $\boldsymbol{F}_m(t)$ refer to the mooring forces; $\boldsymbol{h}(t)$ is the retardation function matrix, which can be expressed as (Cao et al., 2020):

$$\boldsymbol{h}(t) = \frac{2}{\pi} \int_0^\infty \boldsymbol{B}(\omega) cos(\omega t) d\omega \qquad (30)$$

where $\boldsymbol{B}(\omega)$ represents the radiation damping matrix at the angular frequency of ω.

3. Features of the floating energy harvesting platform concept

A floating energy harvesting platform concept is proposed in this paper, which integrates multiple point-absorber WECs onto a semi-submersible platform system. The main parameters of the semi-submersible platform (Zhang et al., 2023a), mooring system (Zhang et al., 2023b) and WEC are listed in Tables 1–3, respectively. Fig. 1 depicts the floating energy harvesting platform. Additionally, the WEC spacing is defined as L. The current study focuses on the effects of different WEC spacings on the performance of this hybrid system. Accordingly, five different values were set for L, referred to as Models

(a) Top view
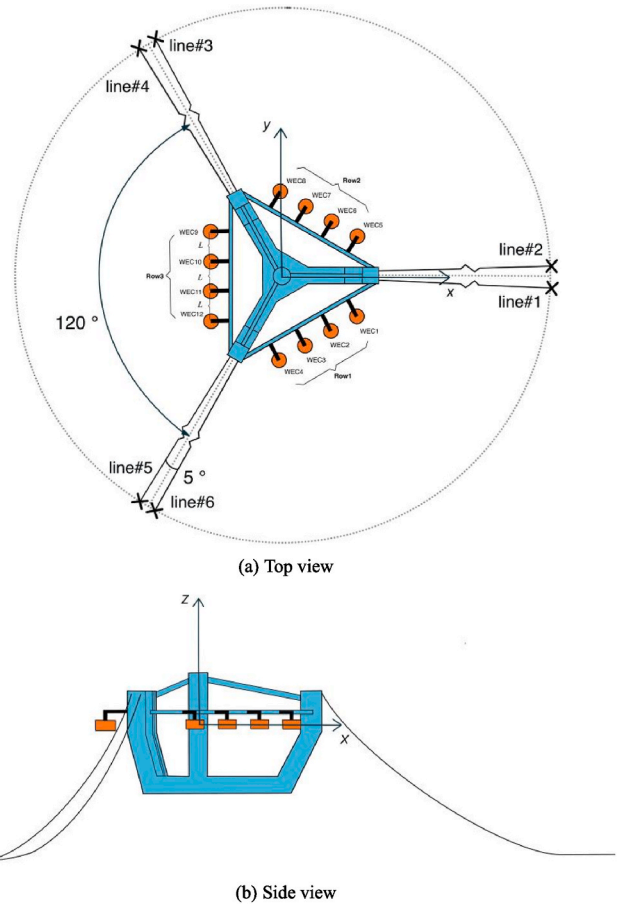
(b) Side view

Fig. 1. (a) Top view and (b) side view of the floating energy harvesting platform.

Table 4
Definition of five models (D: Diameter of the WEC).

L	Model
2 D	1
2.25 D	2
2.5 D	3
2.75 D	4
3 D	5

1–5, as shown in Table 4.

This hybrid system captures the energy through the relative vertical motion between the platform and WEC array, which drives the power take-off (PTO) device. In this paper, the PTO device is simplified as a hinged joint with rotational damping. Moreover, under severe wave conditions, the hinged joints between the platform and WEC array are locked to prevent the huge wave forces from damaging the PTO device. To clearly illustrate the motion and energy conversion modes, Appendix A provides the mathematical expressions for $\boldsymbol{C}_{PTO}$ and $\boldsymbol{H}$ in Eq. (29). Meanwhile, it also derives the formulas to calculate the captured energy.

4. Results and discussion

For the accuracy of the current study, the numerical models should be validated. Fig. 2 shows the RAOs (response amplitude operators) of the platform motions in both numerical and experimental studies (Wu et al., 2024a; Wu et al., 2024c; Wu et al., 2024c). As for the WEC prototype in this paper, He et al. (2023) conducted the experimental study. Fig. 3 illustrates the heave RAOs of the WEC in both numerical and
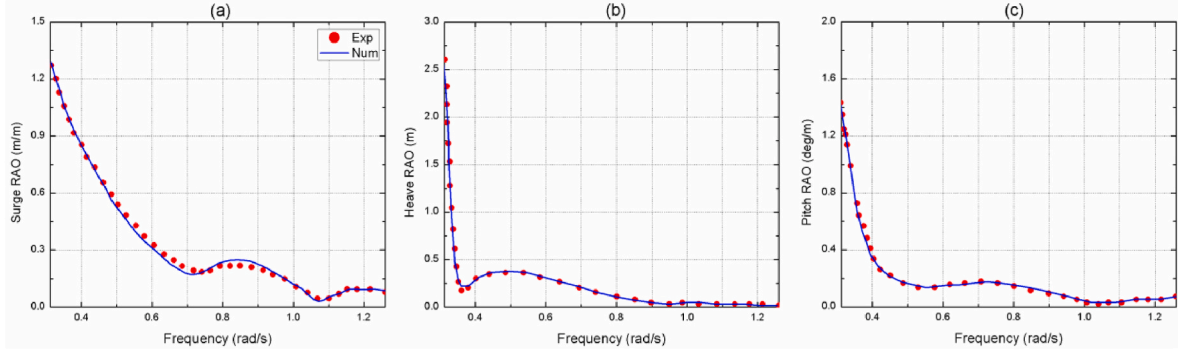
Fig. 2. The surge (a), heave (b) and pitch (c) RAOs of the platform in both numerical and experimental analysis.
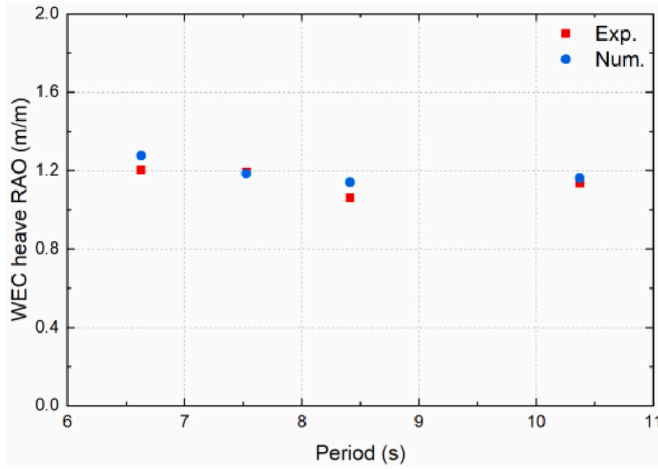
Fig. 3. The heave RAOs of the WEC in both numerical and experimental analysis.

experimental analysis. The figures implies that the numerical data aligns well with the experimental results, indicating that the models of the semi-submersible platform and WEC in the current study are reliable.

This section investigates the energy capture and dynamic responses of five floating energy harvesting platform models. Firstly, their energy conversion performance and the RAOs of the platform systems are investigated under the wave conditions with average height ($H = 3.8$ m) and typical period range ($T = 5$–12 s). Then, a comparative study of the performance of these models is performed under average wave condition ($H = 3.8$ m, $T = 8.3$ s) and severe wave condition ($H = 8.1$ m, $T = 11.4$ s). It should be noted that the wave incidence angle keeps at $0°$.

4.1. Energy absorption

The investigation in this section is conducted from three perspectives: the individual WEC, WEC row, and WEC array. Regarding energy harvesting performance of the individual WEC, WECs 1–4 and WECs 11–12 are chosen. Regarding the WEC row, the energy absorption of Rows 1 and 3 is analyzed. The rationale for the selections counts on the symmetry of the hybrid system about the wave incidence angle. Notably, the concept of the influence factor is introduced to assess the effects of hydrodynamic interactions on the absorbed power. The calculation formula for the influence factor can be expressed as:

$$q_s = \frac{P_m^i}{P_s^i} \tag{31}$$

$$q_r = \frac{\sum_{i=j+1}^{j+4} P_m^i}{\sum_{i=j+1}^{j+4} P_s^i}, j = 0 \ or \ 8 \tag{32}$$

$$q_a = \frac{\sum_{i=1}^{12} P_m^i}{\sum_{i=1}^{12} P_s^i} \tag{33}$$

where q_s, q_r and q_a are the influence factors of the individual WEC, WEC row and WEC array, respectively; P_m^i denotes the absorbed power of the i-th WEC in the hybrid models, while P_s^i is the captured power of the i-th WEC when it operates alone.

4.1.1. Individual WEC

First of all, the energy absorption of the individual WECs in different models is analyzed. Fig. 4 presents the energy absorbed by WECs 1–4 and WECs 11–12 under various wave periods. From Fig. 4(a), it can be observed that in Models 1–3, WEC1 captures the most power at T = 8 s, while in Models 4 and 5, the peak energy absorption occurs at $T = 12$ s and 11 s, respectively. Meanwhile, for all five models, WEC1 absorbs the least power at $T = 5$ s. Notably, the maximum and minimum energy absorption for WEC1 is observed in Models 2 and 1, respectively. In Fig. 4(b), it is evident that except for $T = 5$–7 s, WEC2 demonstrates an increasing trend in energy conversion performance across Models 1–5. However, at $T = 6$ s, the trend reverses. Additionally, at $T = 5$ s, WEC2 harvests the most power in Model 5 and the least in Model 3. At $T = 7$ s, it captures the most power in Model 4 and the least in Model 1. Fig. 4(c) shows that WEC3 achieves its best energy capture performance at $T = 6$–7 s and performs the worst at $T = 11$–12 s across the five models. Furthermore, the maximum and minimum energy absorption occurs in Models 4 and 1, respectively. In Fig. 4(d), it can be observed that at $T = 5$ s and 8 s, the energy absorption of WEC4 gradually decreases from Models 1 to 5. Additionally, at $T = 5$ s, WEC4 captures the most power in Model 5 and the least in Model 2. At $T = 8$ s, it captures the most and least power in Models 2 and 5, respectively. From Fig. 4(e), it is apparent that at large wave periods ($T = 10$–12 s), the energy conversion performance of WEC11 exhibits an increasing trend across Models 1–5. However, at $T = 6$ s, the trend is reversed. Furthermore, in each model, WEC11 captures the most power at $T = 5$ s and the least at $T = 7$ s. Interestingly, in Model 3, WEC11 shows the worst and best performance at $T = 5$ s and 7 s, respectively, compared to other models. In Fig. 4(f), WEC12 shows an increasing trend in energy absorption across Models 1–5 for $T = 7$–8 s and 10–12 s. Additionally, at $T = 5$ s, WEC12 harvests the most power in Model 5 and the least in Model 3. At T = 6 s, it captures the most and least power in Models 3 and 1, respectively. Furthermore, at $T = 9$ s, WEC12 performs the best in Model 4 and the worst in Model 1. Notably, similar to WEC11, WEC12 achieves its
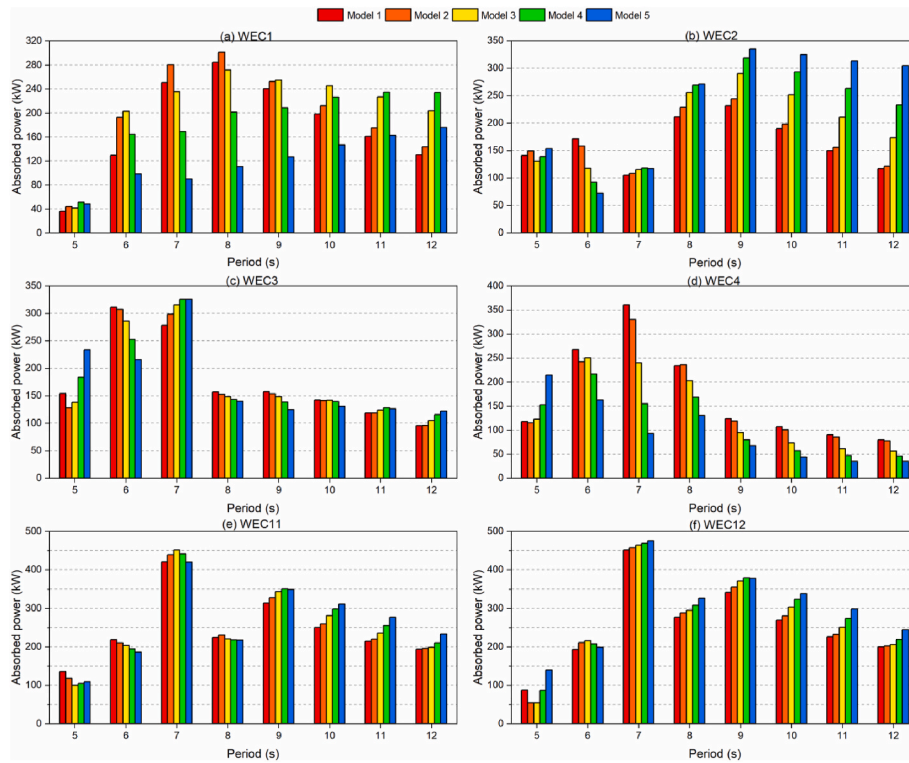
Fig. 4. Captured power of an individual WEC in five models under various wave periods.

maximum and minimum energy absorption at $T = 5$ s and 7 s, respectively, in each model.

Since the PTO system is stimulated by the relative vertical motion between the platform and WEC, the motion amplitude and phase are critical factors influencing the energy harvesting performance of the WEC. To better explain the difference in the absorbed power of the individual WEC across five models, this study provides the heave responses of the platform and WEC1 at $T = 8$ s, as shown in Fig. 5. The figure demonstrates that the platform response amplitude in Model 1 is slightly larger than that in Model 2, whereas the opposite is true for WEC1. Furthermore, the phase difference between the platform and WEC1 in Model 1 is almost consistent with that in Model 2. Based on these observations, it can be inferred that the relative heave response between the platform and WEC1 is larger in Model 2 than that in Model 1. In Model 3, the platform heave response is larger than that in Models 1 and 2, while for WEC1, the situation is reversed. Meanwhile, the phase difference between the platform and WEC1 in Model 3 is smaller than that in Models 1 and 2. This means that the relative heave response between the platform and WEC1 is smaller in Model 3 than that in Models 1 and 2. Interestingly, the platform heave response shows an increasing trend across Models 3–5, while for WEC1, the opposite trend is observed. Additionally, the phase difference between the platform and WEC1 follows the same trend as the platform heave response across Models 3–5. This suggests that the relative heave response between the platform and WEC1 tends to decrease across Models 3–5. Based on the above analysis, it is inferred that at $T = 8$ s, WEC1 achieves the best energy capture performance in Model 2, while it is with a gradual decline in the energy absorption across Models 3–5. Additionally, its absorbed power in Model 1 is only second to that in Model 2. These inferences are corroborated by the relevant data in Fig. 4(a).

To investigate the impact of hydrodynamic interactions on the energy absorption of the individual WEC, Fig. 6 illustrates the influence factors of each WEC in different models. In Fig. 6(a), it shows that at $T = 5$–6 s, the hydrodynamic interactions negatively affect the energy conversion of WEC1. Moreover, at $T = 7$–9 s, Models 4 and 5 show a

negative contribution to the energy absorption of WEC1, while Models 1 and 2 exhibit a positive impact. For $T = 7$ s, Model 3 slightly diminishes the energy absorption of WEC1. Furthermore, at large wave periods ($T = 10$–12 s), Models 3 and 4 enhance the energy absorption of WEC1, while Model 1 has the opposite effects. In Fig. 6(b), it can be seen that for $T = 5$–7 s, the hydrodynamic interactions reduce the absorbed power of WEC2. Specifically, at $T = 6$ s, the negative influence of hydrodynamic interactions increases progressively across Models 1–5. Additionally, at $T = 8$ s and $T = 10$–12 s, Models 1 and 2 reduce the energy absorption of WEC2, whereas Models 3–5 enhance it. Notably, at $T = 9$ s, the positive impact of hydrodynamic interactions gradually intensifies across Models 1 to 5. From Fig. 6(c), it is evident that at $T = 8$–12 s, all models diminish the absorbed power of WEC3. Particularly, at $T = 8$–10 s, the negative influence of hydrodynamic interactions progressively increases across Models 1–5, while for $T = 11$–12 s, the opposite trend is observed. Additionally, at $T = 7$ s, the hydrodynamic interactions have a positive impact, which becomes stronger from Model 1 to Model 5. Furthermore, at $T = 5$ s, only Models 4 and 5 contribute positively to the energy absorption of WEC3, whereas at $T = 6$ s, only Model 5 negatively affects its performance. In Fig. 6(d), it can be observed that, similar to WEC3, all models reduce WEC4's energy absorption for $T = 8$–12 s. Meanwhile, the negative influence of hydrodynamic interactions increases across Models 1–5. At $T = 5$ s, only Model 5 enhances the energy absorption of WEC4. Additionally, for $T = 6$–7 s, Models 1 and 2 improve the energy capture performance of WEC4. Notably, Model 3 also positively contributes to the energy absorption of WEC4. From Fig. 6(e), it is evident that at $T = 8$ s, none of the models benefits the energy absorption of WEC11; however, for other wave periods, the opposite is true. Furthermore, at $T = 9$–12 s, the positive impact of hydrodynamic interactions increases progressively across Models 1–5, whereas at $T = 6$ s, the opposite trend occurs. In Fig. 6(f), it is shown that for $T = 6$–12 s, all models benefit the energy absorption of WEC12. Meanwhile, the contribution of hydrodynamic interactions increases progressively across Models 1–5. Additionally, at $T = 5$ s, only Models 2 and 3 negatively affect the energy absorption of WEC12.
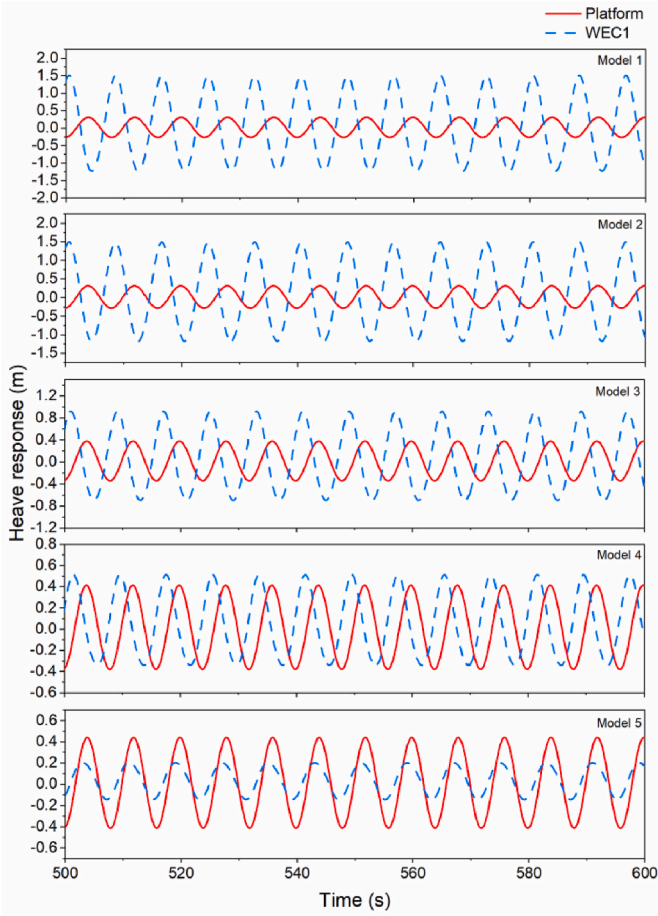
Fig. 5. Heave responses of the platform and WEC1 in different models at $T = 8$ s.

4.1.2. WEC row

Then, the captured power of WEC row in different models is analyzed. Fig. 7 illustrates the power absorbed by Rows 1 and 3 under various wave periods. Fig. 7(a) shows that in Models 1–4, the absorbed power of Row1 exhibits a trend of initially increasing and then decreasing across the wave period range of 5–12 s. For Models 1–3, the energy capture performance of Row1 is optimal at $T = 7$ s, whereas for Model 4, the optimal performance occurs at $T = 8$ s. In Model 5, the absorbed power of Row1 reaches its maximum and minimum at $T = 9$ s and 6 s, respectively. Additionally, within the wave period range of 6–11 s, the absorbed power of Row1 across Models 1–5 follows a trend of initially increasing and then decreasing. Specifically, for $T = 6–8$ s, the energy harvesting performance of Row1 is optimal in Model 2, while for $T = 10–11$ s, the same situation occurs in Model 4. At $T = 9$ s, Row1 captures the most power in Model 3. Furthermore, at $T = 5$ s, Row1 absorbs the most and least power in Models 5 and 3, respectively. Notably, at $T = 12$ s, the absorbed power of Row1 increases across Models 1–5. Fig. 7(b) demonstrates that for Models 1–5, Row3 harvests the most and least power at $T = 7$ s and 5 s, respectively. Notably, at $T = 9$ s, the energy conversion performance of Row3 is also outstanding, second only to its performance at $T = 7$ s. At large wave periods (10–12 s), the power absorbed by Row3 shows an upward trend across Models 1–5. Furthermore, for $T = 6–7$ s and 9 s, the energy capture performance of Row3 first strengthens and then weakens across Models 1–5, while at $T = 5$ s, the trend is reversed. Meanwhile, for $T = 5–7$ s and 9 s, Row3 captures the most power in Models 5, 2, 3, and 4, respectively. Additionally, at $T = 8$ s, the energy conversion of Row3 is the best in Model 5 and the worst in Model 1.

To explore the influence of the hydrodynamic interactions on the energy absorption of WEC rows, Fig. 8 illustrates the influence factors for WEC rows in different models. In Fig. 8(a), it demonstrates that at $T = 5$ s and 8–12 s, the hydrodynamic interactions negatively affect the energy absorption of Row1 in all models. At $T = 10–12$ s, Model 1 exhibits the most negative impact on the energy absorption of Row1. Meanwhile, at $T = 8–9$ s, Model 5 demonstrates the most adverse effects on the energy capture of Row1, whereas at $T = 5$ s, the situation is reversed. Additionally, at $T = 6$ s, only Model 2 positively contributes to the energy conversion performance of Row1, while at $T = 7$ s, the effects of hydrodynamic interactions are also positive in Model 1. Furthermore, for $T = 6–7$ s, the negative impact of hydrodynamic interactions increases progressively across Models 3–5. Fig. 8(b) indicates that across the entire wave period range, the hydrodynamic interactions positively contribute to the energy absorption of Row3 in all models. At $T = 8–12$ s, the contribution of hydrodynamic interactions increases progressively across Models 1–5. Additionally, at $T = 5$ s, the contributions of different models to the energy capture of Row3 vary significantly, whereas at $T = 6–8$ s, the differences are relatively small. Moreover, the positive impact of hydrodynamic interactions reaches its maximum and minimum at $T = 7$ s and 8 s, respectively.

4.1.3. WEC array

Finally, the energy absorption of the WEC array in five models is analyzed. Fig. 9 presents the power absorbed by the WEC array under various wave periods. The figure reveals that in all models, the harvested power of the WEC array reaches its maximum and minimum at $T = 7$ s and 5 s, respectively. Additionally, at $T = 9$ s, the captured power of the WEC array is relatively much, second only to that at $T = 7$ s. Furthermore, at $T = 5$ s, the absorbed power of the WEC array initially decreases and then increases across Models 1–5, while for $T = 6–10$ s, the trend is reversed. Firstly, at $T = 5$ s, the WEC array captures the most power in Model 5 and the least in Model 3. Then, at $T = 6–8$ s, the energy capture of the WEC array is optimal in Model 2 and poorest in Model 5. Moreover, at $T = 9$ s, Model 3 contributes the most to the energy capture of the WEC array, whereas at $T = 10$ s, Model 4 shows the best performance. Notably, at $T = 11–12$ s, the captured power of the WEC array exhibits an increasing trend across Models 1–5.

To investigate the effects of hydrodynamic interactions on the energy absorption of the WEC array, Fig. 10(a) presents the influence factors of the WEC array in five models. Additionally, Fig. 10(b) illustrates the capture width ratio (CWR) of the WEC array, in order to quantify the energy conversion efficiency. The formula for calculating the capture width ratio can be expressed as:

$$\text{CWR} = \frac{P_a}{P_w \bullet D \bullet N} = \frac{\sum_{i=1}^{12} P_m^i}{\frac{\rho g^2 H^2 T}{32\pi} \bullet 8 \bullet 12} \tag{34}$$

where P_a represents the total power captured by the WEC array; P_w denotes the wave energy per unit width; N is the number of WECs in the WEC array.

Fig. 10(a) demonstrates that at $T = 7$ s and 9 s, the hydrodynamic interactions in Models 1–5 are favorable for the energy absorption of the WEC array, whereas for $T = 8$ s, the situation is reversed. Additionally, at $T = 5$ s, only Model 5 is favorable for the energy absorption of the WEC array, while for $T = 6$ s, Models 1–3 are beneficial. Moreover, at large wave periods (10–12 s), Models 4–5 enhance the energy capture of the WEC array, while Models 1–2 have the opposite effects. It is worth noting that in Model 3, the influence of hydrodynamic interactions transitions from positive to negative across the wave period range ($T = 10–12$ s). In Fig. 10(b), it can be seen that the capture width ratio (CWR) of the WEC array generally ranges from 0.1 to 0.4. Within the wave period range ($T = 5–12$ s), the energy harvesting efficiency of the WEC array reaches the highest at $T = 12$ s and the lowest at $T = 7$ s. At $T = 5$ s, Model 5 has a notably stronger influence on improving the energy harvesting efficiency of the WEC array, compared to other four models.
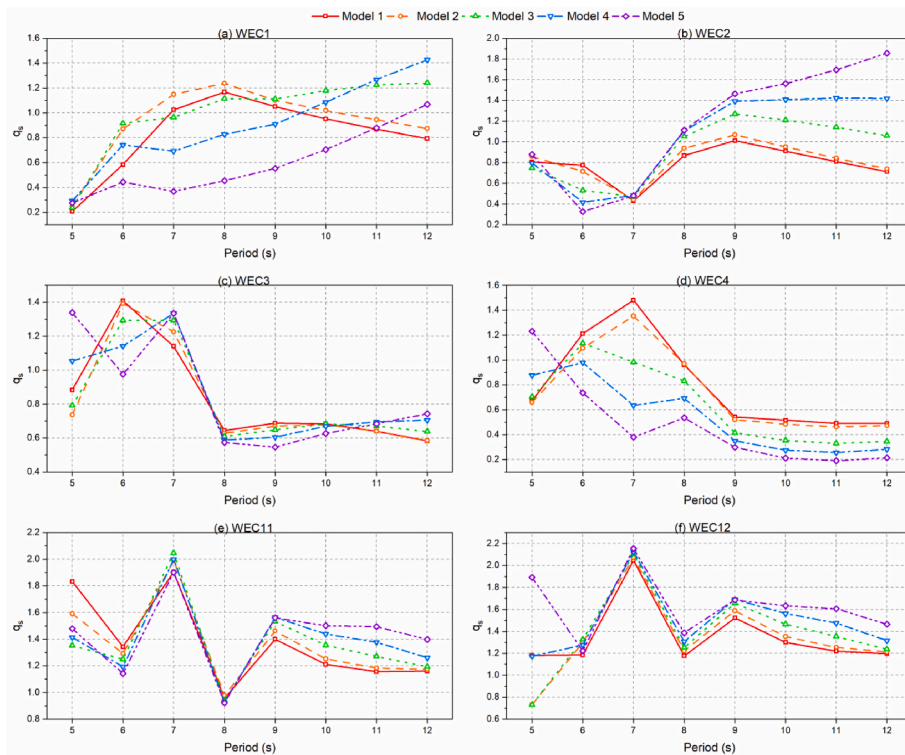
Fig. 6. q_s of an individual WEC in five models under various wave periods.
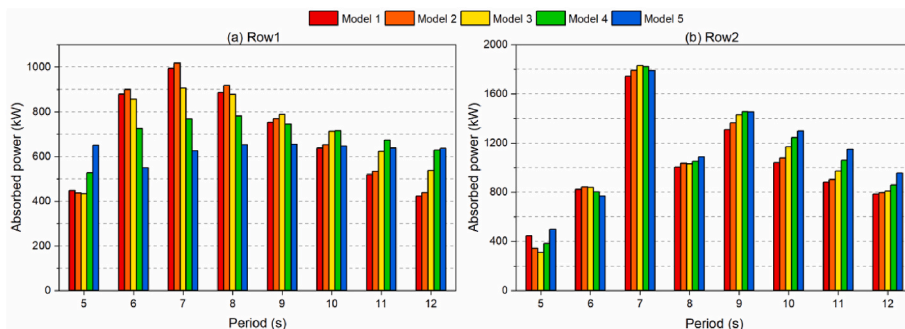
Fig. 7. Captured power of the WEC row in five models under various wave periods.
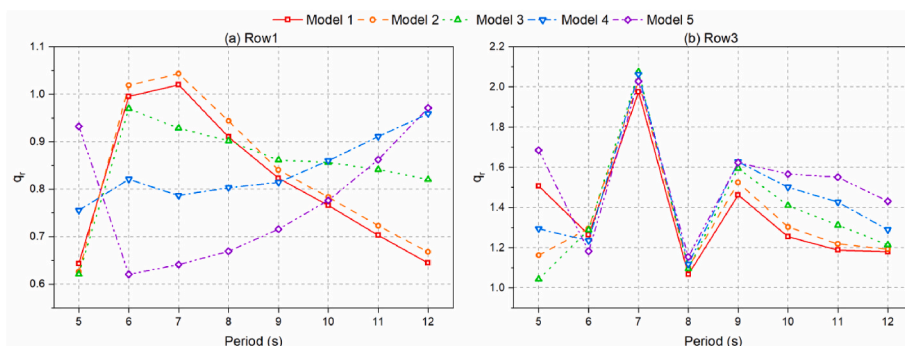
Fig. 8. q_r of the WEC row in five models under various wave periods.
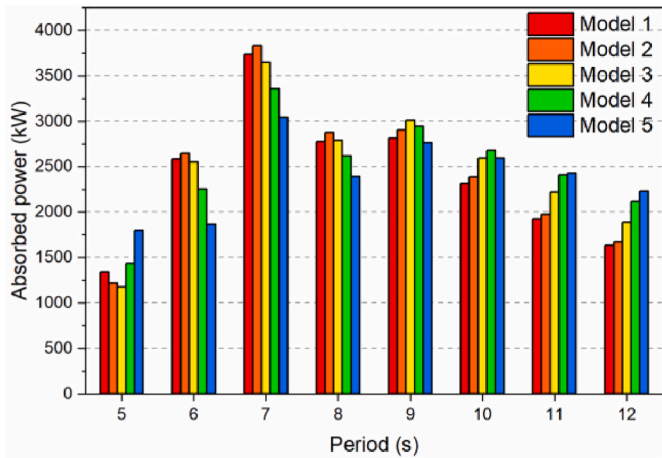
Fig. 9. Captured power of the WEC array in five models under various wave periods.

Additionally, at $T = 6$–8 s, the WEC array captures the most and least power in Models 2 and 5, respectively. Moreover, at large wave periods (10–12 s), the energy harvesting efficiency of the WEC array exhibits an upward trend across Models 1–5. Interestingly, at $T = 9$ s, the energy

capture of the WEC array does not vary significantly across different models.

4.2. RAOs of the platform system

The dynamic responses of the mooring tension and platform motion are crucial for the stability and safety of the floating system. Therefore, this section analyzes these two objects under various wave periods in different models. Figs. 11 and 12 present the RAOs of the platform motion and #5 tension, respectively. Because the hybrid system is symmetric about the wave incident angle, only three DOFs need to be considered for the platform motion: surge, heave, and pitch. As for Fig. 12, it only presents the tension response of #5, which experiences the largest excitation forces in the mooring system.

Fig. 11(a) illustrates that within the wave period range ($T = 5$–6 s), the surge response is significantly smaller than that within the wave period range ($T = 7$–12 s). At $T = 7$ s, the surge response is larger than that at $T = 8$ s, and it shows an increasing trend across the wave period range ($T = 8$–12 s). Particularly, at $T = 9$–12 s, the differences in the surge response across different wave periods become quite pronounced. Additionally, at $T = 5$ s, the surge response increases across Models 1–5, while at $T = 6$ s, the trend is the opposite. For other wave periods, the surge response does not show significant variations between different models. In Fig. 11(b), it shows that the heave response exhibits an
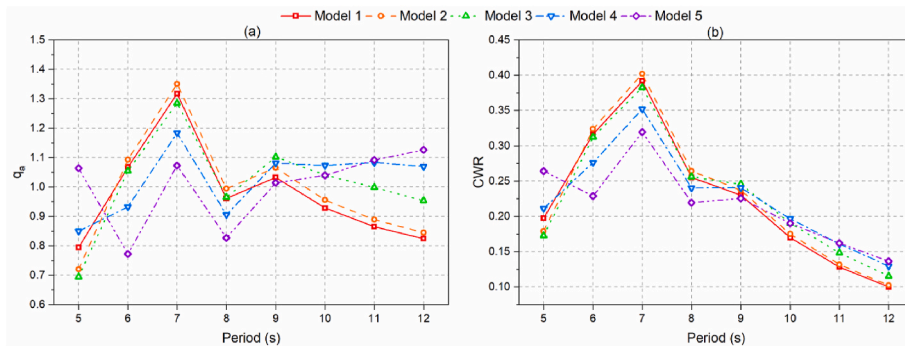
Fig. 10. (a) q_a and (b) CWR of the WEC array in five models under various wave periods.
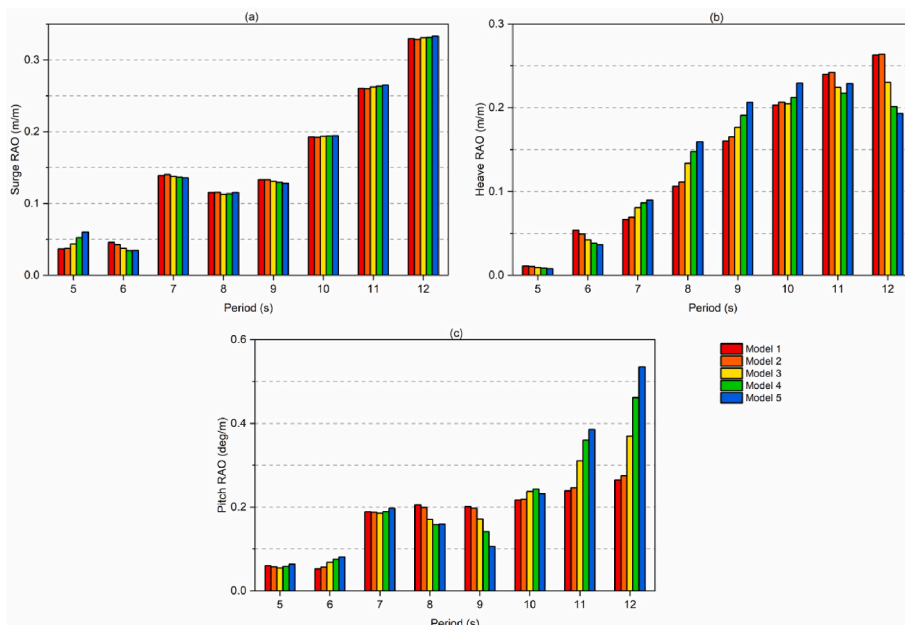
Fig. 11. RAOs of the platform motion in different models under various wave periods.
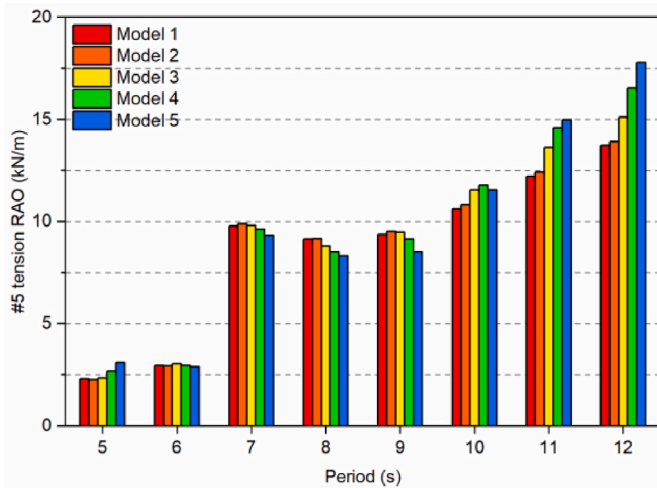
Fig. 12. RAOs of #5 tension in different models under various wave periods.

increasing trend across the wave period range ($T = 5$–12 s) for Models 1–3, whereas for Models 4–5, it increases firstly and then decreases. In Models 4–5, the heave response reaches its maximum at $T = 11$ s and 10 s, respectively. Additionally, for $T = 5$–6 s, the heave response shows a decreasing trend across Models 1–5, whereas the opposite trend occurs for $T = 7$–9 s. Furthermore, at $T = 10$–12 s, the minimum heave response is observed in Models 1, 4, and 5, while the maximum responses are observed in Models 5, 2, and 2. From Fig. 11(c), similar to the surge DOF, the pitch response is significantly larger at $T = 7$–12 s than that at $T = 5$–6 s. For Models 1–2, the pitch response exhibits the upward trend across the wave period range ($T = 7$–12 s), while for Models 3–5, the trend first decreases and then increases. Particularly for large wave periods (10–12 s), the differences in the pitch response across the various wave periods are quite evident for Models 3–5. Moreover, at $T = 6$ s and 11–12 s, the pitch response has an increasing trend across Models 1–5, while at $T = 9$ s, the trend is reversed. For large wave periods (11–12 s), the differences in the pitch response across the different models become significant. As for $T = 5$ s and 7 s, the pitch response does not show significant changes between various models, while for $T = 8$ s and 10 s, the situation is the opposite. Interestingly, at $T = 8$ s and 10 s, the maximum pitch responses are observed in Models 1 and 4, respectively, while the minimum responses occur in Models 4 and 1,
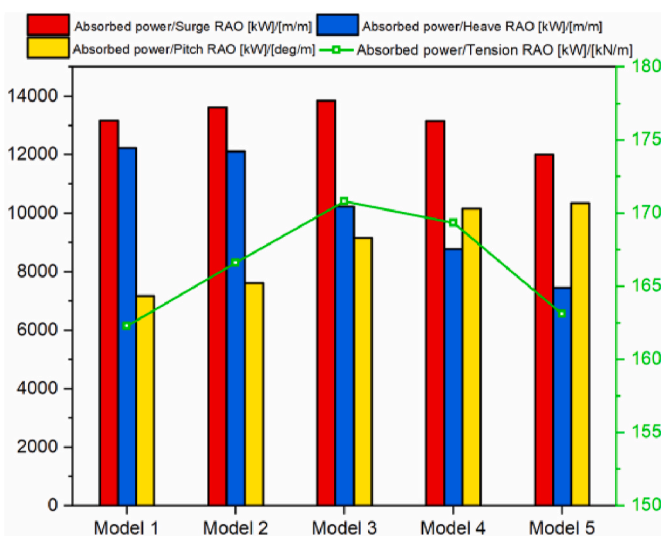
respectively.

From Fig. 12, it demonstrates that similar to the platform motions, the tension response of #5 at $T = 5$–6 s is significantly smaller than that at $T = 7$–12 s. Within the wave period range of 7–12 s, the #5 tension response exhibits a trend of initially decreasing and then increasing, with a notable turning point at $T = 8$ s. Furthermore, at $T = 7$–9 s, the differences in #5 tension responses across various wave periods are relatively insignificant compared to those observed at $T = 9$–12 s. This may be because the sensitivity of the #5 tension response to the wave period becomes particularly pronounced within the range of 9–12 s. Moreover, at $T = 11$–12 s, the #5 tension response demonstrates an increasing trend across Models 1–5, whereas the patterns for other wave periods are relatively complex. At $T = 5$ s, the #5 tension response reaches its maximum and minimum values in Models 5 and 2, respectively. At $T = 6$ s, the feature of the model does not result in noticeable variation in the response. For $T = 7$–9 s, the #5 tension response initially increases and then decreases across Models 1–5, with maximum and minimum values occurring in Models 2 and 5, respectively. At $T = 10$ s, the #5 tension response reaches its maximum and minimum in Models 4 and 1, respectively.

4.3. Performance comparison of different models

This section conducts a comparative study of different models regarding the energy conversion performance under average and severe wave conditions. Under average wave condition, the ratio of total captured power to the RAOs of the platform system is utilized as the performance evaluation criterion. Under severe wave condition, the safety and stability of the hybrid system depend on the dynamic responses of the platform motion and mooring tension. Therefore, the RAOs of the platform system are selected as the basis for the performance comparison.

Fig. 13 illustrates the ratio of total power to the RAOs of the platform system in different models under average wave condition. From the figure, it can be observed that the difference in the ratio of total power to the surge RAO across different models is less significant than that for the heave and pitch motions. However, it is noted that this ratio reaches its maximum and minimum in Models 3 and 5, respectively, indicating that Models 3 and 5 are the best and worst energy conversion designs based on the surge motion. Additionally, the ratio of total power to the heave RAO shows a decreasing trend across Models 1–5, while for the pitch RAO, the trend is the opposite. This suggests that when the heave motion

Fig. 13. Ratios of the total power to RAOs of the platform system in five models under average wave condition.
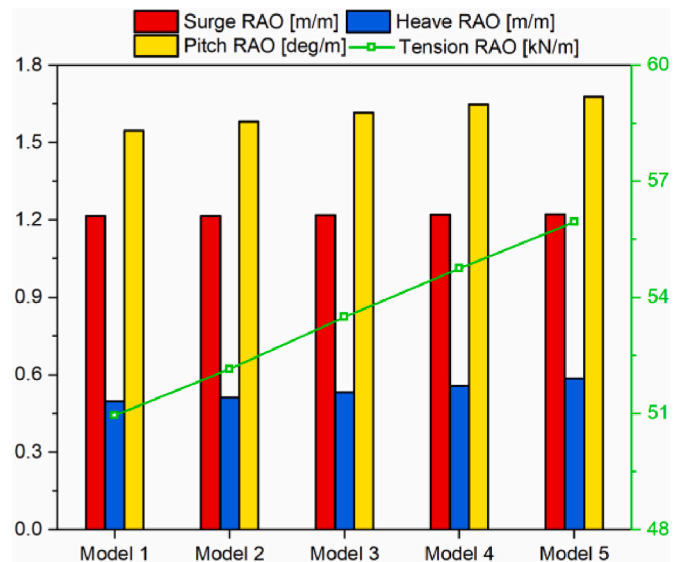
Fig. 14. RAOs of the platform system in five models under severe wave condition.

is considered as a baseline, the energy absorption of the system decreases sequentially from Model 1 to Model 5, whereas the opposite trend occurs for the pitch motion. Furthermore, the ratio of total energy to the tension RAO of #5 reaches its maximum and minimum in Models 3 and 1, respectively, indicating that with the basis of #5 tension, Models 3 and 1 contribute the most and least to the energy absorption of the system. In summary, the optimal model under average wave condition varies depending on the performance evaluation criterion.

Fig. 14 presents the RAOs of the platform system under extreme wave condition in different models. From the figure, it can be observed that the surge RAO remains almost constant across the different models. Additionally, for the heave and pitch motion, as well as #5 tension, the RAOs show an increasing trend from Model 1 to Model 5. It is worth noting that the differences in the heave RAO in the models are relatively small. Therefore, regarding the performance of this hybrid system under severe wave condition, it can be inferred that Models 1 and 5 are the best and worst designs, respectively.

5. Conclusion

This paper conducts a numerical analysis of the energy absorption and dynamic behavior for a floating energy harvesting platform with various WEC spacings. After the time-domain motion equation of the hybrid system is established, typical wave periods are considered under average wave height to explore the performance variations of different models. Furthermore, a comparative analysis of the performance under both average and severe wave conditions is carried out. According to the results, several key conclusions are drawn as follows.

1. The energy capture performance of the upstream WECs is the best at $T = 5$ s and the poorest at $T = 7$ s. Meanwhile, at $T = 5$ s, they absorb the least power in Model 3. Additionally, the hydrodynamic interactions contribute most significantly to the energy absorption at $T = 7$ s, with minimal variation across different models.
2. The upstream WEC row absorbs the most power at $T = 5$ s and the least at $T = 7$ s. Additionally, in Model 3, its energy capture performance is the worst at $T = 5$ s and the best at $T = 7$ s. Furthermore, across the wave period range of 5–12 s, the hydrodynamic interactions positively affect the energy absorption in all five models. Notably, the positive effects vary insignificantly across different models at $T = 7$ s.
3. The captured power of the WEC array reaches the most at $T = 5$ s and the least at $T = 7$ s. Additionally, at $T = 5$ s and 7 s, it captures the most power in Model 3 and the least in Model 2, respectively. Furthermore, the hydrodynamic interactions enhance the energy

absorption at $T = 7$ s and 9 s but have a detrimental impact at $T = 8$ s. Moreover, the energy harvesting efficiency of the array reaches the highest at $T = 7$ s and the lowest at $T = 12$ s. Notably, at $T = 9$ s, its energy conversion efficiency remains relatively consistent across different models.
4. Overall, the dynamic response of the platform system exhibits an upward trend across the wave period range of 5–12 s. The heave response is obviously affected by the model variation over the entire wave period range, while the surge response is relatively sensitive to the model variation at small wave periods ($T = 5$–6 s). Additionally, the pitch response remains insignificantly unaffected by the model variation at $T = 5$ s and 7 s. Furthermore, the tension response of #5 exhibits a pronounced increasing trend across different models at large wave periods ($T = 11$–12 s).
5. Under average wave condition, the best models are Models 3, 1, 5, and 3 with the surge, heave, pitch and #5 tension as the performance evaluation criteria, respectively. Additionally, under severe sea condition, Models 1 and 5 are the optimal and worst designs, respectively.

The current study emphasizes the effects of hydrodynamic interactions on the performance of the energy harvesting platform. Its analytical framework and methods could provide some insights into the design and optimization of other ocean energy systems.

CRediT authorship contribution statement

Haitao Wu: Writing – original draft, Visualization, Validation, Methodology, Investigation, Formal analysis, Data curation, Conceptualization. **Zhiming Yuan:** Writing – review & editing, Supervision.

Data availability

Data will be made available on request.

Declaration of competing interest

The authors declare that they have no known competing financial interests or personal relationships that could have appeared to influence the work reported in this paper.

Appendix A

For the energy harvesting system shown in Fig. 1, it comprises 13 floating bodies and 12 hinge constraints. Consequently, the constraint matrices H_1 and H_2 for this hybrid system under operational and locked conditions can be respectively expressed as:

$$
H_1 = \begin{bmatrix}
H^1_{P,W1} & H^1_{W1} & 0 & 0 & 0 & 0 & 0 & 0 & 0 & 0 & 0 & 0 & 0 \\
H^1_{P,W2} & 0 & H^1_{W2} & 0 & 0 & 0 & 0 & 0 & 0 & 0 & 0 & 0 & 0 \\
H^1_{P,W3} & 0 & 0 & H^1_{W3} & 0 & 0 & 0 & 0 & 0 & 0 & 0 & 0 & 0 \\
H^1_{P,W4} & 0 & 0 & 0 & H^1_{W4} & 0 & 0 & 0 & 0 & 0 & 0 & 0 & 0 \\
H^1_{P,W5} & 0 & 0 & 0 & 0 & H^1_{W5} & 0 & 0 & 0 & 0 & 0 & 0 & 0 \\
H^1_{P,W6} & 0 & 0 & 0 & 0 & 0 & H^1_{W6} & 0 & 0 & 0 & 0 & 0 & 0 \\
H^1_{P,W7} & 0 & 0 & 0 & 0 & 0 & 0 & H^1_{W7} & 0 & 0 & 0 & 0 & 0 \\
H^1_{P,W8} & 0 & 0 & 0 & 0 & 0 & 0 & 0 & H^1_{W8} & 0 & 0 & 0 & 0 \\
H^1_{P,W9} & 0 & 0 & 0 & 0 & 0 & 0 & 0 & 0 & H^1_{W9} & 0 & 0 & 0 \\
H^1_{P,W10} & 0 & 0 & 0 & 0 & 0 & 0 & 0 & 0 & 0 & H^1_{W10} & 0 & 0 \\
H^1_{P,W11} & 0 & 0 & 0 & 0 & 0 & 0 & 0 & 0 & 0 & 0 & H^1_{W11} & 0 \\
H^1_{P,W12} & 0 & 0 & 0 & 0 & 0 & 0 & 0 & 0 & 0 & 0 & 0 & H^1_{W12}
\end{bmatrix}_{(4\times8+5\times4)\times(6\times13)}
\tag{A1}
$$

$$H_2 = \begin{bmatrix} H^2_{P,W1} & H^2_{W1} & 0 & 0 & 0 & 0 & 0 & 0 & 0 & 0 & 0 & 0 & 0 \\ H^2_{P,W2} & 0 & H^2_{W2} & 0 & 0 & 0 & 0 & 0 & 0 & 0 & 0 & 0 & 0 \\ H^2_{P,W3} & 0 & 0 & H^2_{W3} & 0 & 0 & 0 & 0 & 0 & 0 & 0 & 0 & 0 \\ H^2_{P,W4} & 0 & 0 & 0 & H^2_{W4} & 0 & 0 & 0 & 0 & 0 & 0 & 0 & 0 \\ H^2_{P,W5} & 0 & 0 & 0 & 0 & H^2_{W5} & 0 & 0 & 0 & 0 & 0 & 0 & 0 \\ H^2_{P,W6} & 0 & 0 & 0 & 0 & 0 & H^2_{W6} & 0 & 0 & 0 & 0 & 0 & 0 \\ H^2_{P,W7} & 0 & 0 & 0 & 0 & 0 & 0 & H^2_{W7} & 0 & 0 & 0 & 0 & 0 \\ H^2_{P,W8} & 0 & 0 & 0 & 0 & 0 & 0 & 0 & H^2_{W8} & 0 & 0 & 0 & 0 \\ H^2_{P,W9} & 0 & 0 & 0 & 0 & 0 & 0 & 0 & 0 & H^2_{W9} & 0 & 0 & 0 \\ H^2_{P,W10} & 0 & 0 & 0 & 0 & 0 & 0 & 0 & 0 & 0 & H^2_{W10} & 0 & 0 \\ H^2_{P,W11} & 0 & 0 & 0 & 0 & 0 & 0 & 0 & 0 & 0 & 0 & H^2_{W11} & 0 \\ H^2_{P,W12} & 0 & 0 & 0 & 0 & 0 & 0 & 0 & 0 & 0 & 0 & 0 & H^2_{W12} \end{bmatrix}_{(6\times12)\times(6\times13)} \tag{A2}$$

where,

$$H^1_{P,Wi} = \begin{bmatrix} 1 & 0 & 0 & 0 & z_{P,Wi} & -y_{P,Wi} \\ 0 & 1 & 0 & -z_{P,Wi} & 0 & x_{P,Wi} \\ 0 & 0 & 1 & y_{P,Wi} & 0 & 0 \\ 0 & 0 & 0 & 0 & -x_{P,Wi}0 & 1 \end{bmatrix}, (i=1\sim8) \tag{A3}$$

$$H^1_{P,Wj} = \begin{bmatrix} 1 & 0 & 0 & 0 & z_{P,Wj} & -y_{P,Wj} \\ 0 & 1 & 0 & -z_{P,Wj} & 0 & x_{P,Wj} \\ 0 & 0 & 1 & y_{P,Wj} & -x_{P,Wj} & 0 \\ 0 & 0 & 0 & 1 & 0 & 0 \\ 0 & 0 & 0 & 0 & 0 & 1 \end{bmatrix}, (j=9-12) \tag{A4}$$

$$H^1_{Wi} = \begin{bmatrix} -1 & 0 & 0 & 0 & -z_{Wi} & y_{Wi} \\ 0 & -1 & 0 & z_{Wi} & 0 & -x_{Wi} \\ 0 & 0 & -10 & -y_{Wi} & x_{Wi} & 0-1 \\ 0 & 0 & 0 & 0 & 0 & 0 \end{bmatrix}, (i=1\sim8) \tag{A5}$$

$$H^1_{Wj} = \begin{bmatrix} -1 & 0 & 0 & 0 & -z_{Wj} & y_{Wj} \\ 0 & -1 & 0 & z_{Wj} & 0 & -x_{Wj} \\ 0 & 0 & -1 & -y_{Wj} & x_{Wj} & 0 \\ 0 & 0 & 0 & -1 & 0 & 0 \\ 0 & 0 & 0 & 0 & 0 & -1 \end{bmatrix}, (j=9\sim12) \tag{A6}$$

$$H^2_{P,Wk} = \begin{bmatrix} 1 & 0 & 0 & 0 & z_{P,Wk} & -y_{P,Wk} \\ 0 & 1 & 0 & -z_{P,Wk} & 0 & x_{P,Wk} \\ 0 & 0 & 1 & y_{P,Wk} & -x_{P,Wk} & 0 \\ 0 & 0 & 0 & 1 & 0 & 0 \\ 0 & 0 & 0 & 0 & 1 & 0 \\ 0 & 0 & 0 & 0 & 0 & 1 \end{bmatrix}, (k=1-12) \tag{A7}$$

$$H^2_{Wk} = \begin{bmatrix} -1 & 0 & 0 & 0 & -z_{Wk} & y_{Wk} \\ 0 & -1 & 0 & z_{Wk} & 0 & -x_{Wk} \\ 0 & 0 & -1 & -y_{Wk} & x_{Wk} & 0 \\ 0 & 0 & 0 & -1 & 0 & 0 \\ 0 & 0 & 0 & 0 & 0 & 0 \\ 0 & 0 & 0 & 0 & -10 & 0-1 \end{bmatrix}, (k=1\sim12) \tag{A8}$$

where $\left(x_{P,Wi\ or\ j\ or\ k}, y_{P,Wi\ or\ j\ or\ k}, z_{P,Wi\ or\ j\ or\ k}\right)$ represents the coordinates of the i, j or k-th hinge constraints in the platform body-fixed coordinate system; $\left(x_{Wi\ or\ j\ or\ or\ k}, y_{Wi\ or\ j\ or\ k}, z_{Wi\ or\ j\ or\ k}\right)$ denotes the coordinates of the i, j or k-th hinge point in the WEC(i or j or k) body-fixed coordinate system.

Additionally, under the operational conditions, the PTO damping matrix can be expressed as:

$$
C_{PTO} = \begin{bmatrix}
C'_{pto} & -C_{pto1} & -C_{pto1} & -C_{pto1} & -C_{pto1} & -C_{pto2} & -C_{pto2} & -C_{pto2} & -C_{pto2} & -C_{pto3} & -C_{pto3} & -C_{pto3} & -C_{pto3} \\
-C_{pto1} & C_{pto1} & 0 & 0 & 0 & 0 & 0 & 0 & 0 & 0 & 0 & 0 & 0 \\
-C_{pto1} & 0 & C_{pto1} & 0 & 0 & 0 & 0 & 0 & 0 & 0 & 0 & 0 & 0 \\
-C_{pto1} & 0 & 0 & C_{pto1} & 0 & 0 & 0 & 0 & 0 & 0 & 0 & 0 & 0 \\
-C_{pto2} & 0 & 0 & 0 & C_{pto2} & 0 & 0 & 0 & 0 & 0 & 0 & 0 & 0 \\
-C_{pto2} & 0 & 0 & 0 & 0 & C_{pto2} & 0 & 0 & 0 & 0 & 0 & 0 & 0 \\
-C_{pto2} & 0 & 0 & 0 & 0 & 0 & C_{pto2} & 0 & 0 & 0 & 0 & 0 & 0 \\
-C_{pto2} & 0 & 0 & 0 & 0 & 0 & 0 & C_{pto2} & 0 & 0 & 0 & 0 & 0 \\
-C_{pto3} & 0 & 0 & 0 & 0 & 0 & 0 & 0 & C_{pto3} & 0 & 0 & 0 & 0 \\
-C_{pto3} & 0 & 0 & 0 & 0 & 0 & 0 & 0 & 0 & C_{pto3} & 0 & 0 & 0 \\
-C_{pto3} & 0 & 0 & 0 & 0 & 0 & 0 & 0 & 0 & 0 & C_{pto3} & 0 & 0 \\
-C_{pto3} & 0 & 0 & 0 & 0 & 0 & 0 & 0 & 0 & 0 & 0 & C_{pto3}
\end{bmatrix}_{(10\times6)\times(10\times6)} \tag{A9}
$$

where,

$$
C_{pto1} = \begin{bmatrix}
0 & 0 & 0 & 0 & 0 & 0 \\
0 & 0 & 0 & 0 & 0 & 0 \\
0 & 0 & 0 & 0 & 0 & 0 \\
0 & 0 & 0 & \frac{3}{4}c_p & \frac{\sqrt{3}}{4}c_p & 0 \\
0 & 0 & 0 & \frac{\sqrt{3}}{4}c_p & \frac{1}{4}c_p & 0 \\
0 & 0 & 0 & 0 & 0 & 0
\end{bmatrix} \tag{A10}
$$

$$
C_{pto2} = \begin{bmatrix}
0 & 0 & 0 & 0 & 0 & 0 \\
0 & 0 & 0 & 0 & 0 & 0 \\
0 & 0 & 0 & 0 & 0 & 0 \\
0 & 0 & 0 & \frac{3}{4}c_p & -\frac{\sqrt{3}}{4}c_p & 0 \\
0 & 0 & 0 & -\frac{\sqrt{3}}{4}c_p & \frac{1}{4}c_p & 0 \\
0 & 0 & 0 & 0 & 0 & 0
\end{bmatrix} \tag{A11}
$$

$$
C_{pto3} = \begin{bmatrix}
0 & 0 & 0 & 0 & 0 & 0 \\
0 & 0 & 0 & 0 & 0 & 0 \\
0 & 0 & 0 & 0 & 0 & 0 \\
0 & 0 & 0 & 0 & 0 & 0 \\
0 & 0 & 0 & 0 & c_p & 0 \\
0 & 0 & 0 & 0 & 0 & 0
\end{bmatrix} \tag{A12}
$$

$$
C'_{pto} = 4\left(C_{pto1} + C_{pto2} + C_{pto3}\right) = \begin{bmatrix}
0 & 0 & 0 & 0 & 0 & 0 \\
0 & 0 & 0 & 0 & 0 & 0 \\
0 & 0 & 0 & 0 & 0 & 0 \\
0 & 0 & 0 & 6c_p & 0 & 0 \\
0 & 0 & 0 & 0 & 6c_p & 0 \\
0 & 0 & 0 & 0 & 0 & 0
\end{bmatrix} \tag{A13}
$$

where c_p denotes the PTO damping coefficient.

C_{pto1} and C_{pto2} can be derived based on Eqs. (A14) and (A15),

$$
\begin{bmatrix} C_{pto1} & -C_{pto1} \\ -C_{pto1} & C_{pto1} \end{bmatrix} = T'_1 \begin{bmatrix} C & -C \\ -C & C \end{bmatrix} T_1 \tag{A14}
$$

$$
\begin{bmatrix} C_{pto2} & -C_{pto2} \\ -C_{pto2} & C_{pto2} \end{bmatrix} = T'_2 \begin{bmatrix} C & -C \\ -C & C \end{bmatrix} T_2 \tag{A15}
$$

where,

$$
C = \begin{bmatrix}
0 & 0 & 0 & 0 & 0 & 0 \\
0 & 0 & 0 & 0 & 0 & 0 \\
0 & 0 & 0 & 0 & 0 & 0 \\
0 & 0 & 0 & 0 & 0 & 0 \\
0 & 0 & 0 & 0 & c_p & 0 \\
0 & 0 & 0 & 0 & 0 & 0
\end{bmatrix} \tag{A16}
$$

$$T_1 = \begin{bmatrix} \tau_1 & & & \\ & \tau_1 & & \\ & & \tau_1 & \\ & & & \tau_1 \end{bmatrix} \tag{A17}$$

$$T_2 = \begin{bmatrix} \tau_2 & & & \\ & \tau_2 & & \\ & & \tau_2 & \\ & & & \tau_2 \end{bmatrix} \tag{A18}$$

τ_1 and τ_2 are the direction cosine matrices of the local coordinate systems of the individual WECs in Rows 1–2 with respect to the global coordinate system,

$$\tau_1 = \begin{bmatrix} \cos 60° & \cos 150° & \cos 90° \\ \cos 30° & \cos 60° & \cos 90° \\ \cos 90° & \cos 90° & \cos 0° \end{bmatrix} \tag{A19}$$

$$\tau_2 = \begin{bmatrix} \cos 60° & \cos 30° & \cos 90° \\ \cos 150° & \cos 60° & \cos 90° \\ \cos 90° & \cos 90° & \cos 0° \end{bmatrix} \tag{A20}$$

Concerning the captured power (P'_M) of an individual WEC in three WEC rows, the calculation formula should be given separately. Firstly, for the WEC in Row1,

$$P'_M = \frac{1}{T} \int_t^{t+T} \left[\left| \tau^r_{P,Wi} (\dot{\theta}^r_P - \dot{\theta}^r_{Wi}) \right| + \left| \tau^p_{P,Wi} (\dot{\theta}^p_P - \dot{\theta}^p_{Wi}) \right| \right] dt, (i = 1 \sim 4) \tag{A21}$$

$$\tau^r_{P,Wi} = \frac{3}{4} c_{p1} (\dot{\theta}^r_P - \dot{\theta}^r_{Wi}) + \frac{\sqrt{3}}{4} c_{p1} (\dot{\theta}^p_P - \dot{\theta}^p_{Wi}) \tag{A22}$$

$$\tau^p_{P,Wi} = \frac{\sqrt{3}}{4} c_{p1} (\dot{\theta}^r_P - \dot{\theta}^r_{Wi}) + \frac{1}{4} c_{p1} (\dot{\theta}^p_P - \dot{\theta}^p_{Wi}) \tag{A23}$$

where $\tau^p_{P,Wi}$ and $\tau^r_{P,Wi}$ are the pitch and roll torques of the i-th PTO device, respectively; $\dot{\theta}^p_{Wi}$ and $\dot{\theta}^p_P$ are the pitch angular velocities of the i-th WEC and platform, respectively; $\dot{\theta}^r_{Wi}$ and $\dot{\theta}^r_P$ denote the roll angular velocities of the i-th WEC and platform, respectively.

Then, for the WEC in Row2,

$$P'_M = \frac{1}{T} \int_t^{t+T} \left[\left| \tau^r_{P,Wj} (\dot{\theta}^r_P - \dot{\theta}^r_{Wj}) \right| + \left| \tau^p_{P,Wj} (\dot{\theta}^p_P - \dot{\theta}^p_{Wj}) \right| \right] dt, (j = 5 \sim 8) \tag{A24}$$

$$\tau^r_{P,Wj} = \frac{3}{4} c_{p1} (\dot{\theta}^r_P - \dot{\theta}^r_{Wj}) - \frac{\sqrt{3}}{4} c_{p1} (\dot{\theta}^p_P - \dot{\theta}^p_{Wj}) \tag{A25}$$

$$\tau^p_{P,Wj} = -\frac{\sqrt{3}}{4} c_{p1} (\dot{\theta}^r_P - \dot{\theta}^r_{Wj}) + \frac{1}{4} c_{p1} (\dot{\theta}^p_P - \dot{\theta}^p_{Wj}) \tag{A26}$$

Finally, for the WEC in Row3,

$$P'_M = \frac{1}{T} \int_t^{t+T} \left| \tau^p_{P,Wk} (\dot{\theta}^p_P - \dot{\theta}^p_{Wk}) \right| dt, (k = 9 \sim 12) \tag{A27}$$

$$\tau^p_{P,Wk} = c_{p2} (\dot{\theta}^p_P - \dot{\theta}^p_{Wk}) \tag{A28}$$

References

Barltrop, N.D.P., 1988. Floating Structures: A Guide for Design and Analysis, vol. 1. CMPT and OPL.

Cao, Q., Xiao, L., Guo, X., Liu, M., 2020. Second-order responses of a conceptual semi-submersible 10 MW wind turbine using full quadratic transfer functions. Renew. Energy 153, 653–668.

Chen, M., Deng, J., Yang, Y., Zhou, H., Tao, T., Liu, S., Sun, L., Hua, L., 2024. Performance analysis of a floating wind–wave power generation platform based on the frequency domain model. J. Mar. Sci. Eng. 12, 206.

Cheng, Y., Fu, L., Dai, S., Collu, M., Cui, L., Yuan, Z., Incecik, A., 2022. Experimental and numerical analysis of a hybrid WEC-breakwater system combining an oscillating water column and an oscillating buoy. Renew. Sustain. Energy Rev. 169, 112909.

Cui, L., Wu, H., Li, M., Lu, M., Liu, W., Zhang, Z., 2024. Effects of mooring failure on the dynamic behavior of the power capture platforms. Energy 313, 133761.

Cummins, W.E., 1962. The impulse response function and ship motions. Schiff-stechnik 9, 101–109.

Ding, J., Yang, Y., Yu, J., Bashir, M., Ma, L., Li, C., Li, S., 2024. Fully coupled dynamic responses of a barge-type integrated floating wind-wave energy systems with different WEC layouts. Ocean Eng. 313, 119453.

Ghafari, H.R., Ghassemi, H., Abbasi, A., Vakilabadi, K.A., Yazdi, H., He, G., 2022. Novel concept of hybrid wavestar-floating offshore wind turbine system with rectilinear arrays of WECs. Ocean Eng. 262, 112253.

Gu, X., Lin, F., Jiang, W., Xu, J., Liu, J., Wang, K., Tao, T., 2025. Power performance and dynamic characteristics of a 15 MW floating wind turbine with wave energy converter combined concept. Sustain. Horiz 13, 100125.

Gunn, K., Stock-Williams, C., 2012. Quantifying the global wave power resource. Renew. Energy 44, 296–304.

Hall, M., Goupee, A., 2015. Validation of a lumped-mass mooring line model with DeepCwind semisubmersible model test data. Ocean Eng. 104, 590–603.

Havelock, T.H., 1955. Waves due to a floating sphere making periodic heaving oscillations. Proc. Roy. Soc. Lond. 231 (1184), 1–7.

He, G., Liu, C., Zhang, W., Luan, Z., Zhang, Z., 2023. Numerical study of the effect of central platform motion on the wave energy converter array. Ocean Eng. 286, 115483.

Hess, J.L., Smith, A.M.O., 1964. Calculation of nonlifting potential flow about arbitrary three-dimensional bodies. J. Ship Res. 8 (4), 22–44.

Kamarlouei, M., Gaspar, J.F., Calvario, M., Hallak, T.S., Mendes, M.J.G.C., Thiebaut, F., Guedes Soares, C., 2020. Experimental analysis of wave energy converters concentrically attached on a floating offshore platform. Renew. Energy 152, 1171–1185.

Li, Y., Yu, Y., 2012. A synthesis of numerical methods for modeling wave energy converter-point absorbers. Renew. Sustain. Energy Rev. 16 (6), 4352–4364.

Newman, J.N., 1979. The theory of ship motions. Adv. Appl. Mech. 18, 221–283.

Nguyen, H.P., Wang, C.M., Tay, Z.Y., Luong, V.H., 2020. Wave energy converter and large floating platform integration: a review. Ocean Eng. 213, 107768.

Rony, J.S., Karmakar, D., 2024. Hydrodynamic response analysis of a hybrid TLP and heaving-buoy wave energy converter with PTO damping. Renew. Energy 226, 120380.

Shi, X., Liang, B., Du, S., Shao, Z., Li, S., 2022. Wave energy assessment in the China East Adjacent Seas based on a 25-year wave-current interaction numerical simulation. Renew. Energy 199, 1381–1407.

Sun, K., Yi, Y., Zheng, X., Cui, L., Zhao, C., Liu, M., Rao, X., 2021. Experimental investigation of semi-submersible platform combined with point-absorber array. Energy Convers. Manag. 245, 114623.

Sun, L., Taylor, R.E., Choo, Y.S., 2011. Responses of interconnected floating bodies. IES J. Part A Civ. Struct. Eng. 4 (3), 143–156.

Wu, H., Deng, W., Yuan, Z., 2024a. Numerical investigation of the effects of wave–current interaction on the dynamic responses of a floating power harvesting platform. Phys. Fluids 36, 107115.

Wu, H., Yuan, Z., 2024. Numerical investigation of the effects of short-crested irregular waves on the performance of a floating power capture platform. Ocean Eng. 313, 119548.

Wu, H., Zhu, F., Yuan, Z., 2024c. Effects of the WEC shape on the performance of a novel hybrid WEC-FOWT system. Energy 288, 129907.

Zhang, Z., Bu, Y., Wu, H., Wu, L., Cui, L., 2023a. Parametric study of the effects of clump weights on the performance of a novel wind-wave hybrid system. Renew. Energy 219, 119464.

Zhang, Z., Chen, X., Wu, H., Liu, W., Cui, L., 2023b. Numerical study of a novel hybrid system with the Wavestar wave energy converter array and a SPIC semi-submersible floating platform. J. Clean. Prod. 407, 137178.

Zhang, H., Wang, T., Xu, C., Shi, H., Guedes Soares, C., 2023. Analysis on the split absorber integrated with taut-moored floating turbine. Phys. Fluids 35, 087110.

Zhao, X., Xue, F., Chen, L., Göteman, M., Han, D., Geng, J., Sun, S., 2023. Hydrodynamic analysis of a floating platform coupled with an array of oscillating bodies. Ocean Eng. 287, 115439.

Zhou, B., Zheng, Z., Hong, M., Jin, P., Wang, L., Chen, F., 2023. Dynamic and power generation features of A Wind Wave hybrid system consisting of A spar-type wind turbine and an annular wave energy converter in irregular waves. China Ocean Eng. 37 (6), 923–933.